ISSN 1063-7842, Technical Physics, 2019, Vol. 64, No. 10, pp. 1430–1440. © Pleiades Publishing, Ltd., 2019.
Russian Text © The Author(s), 2019, published in Zhurnal Tekhnicheskoi Fiziki, 2019, Vol. 89, No. 10, pp. 1513–1523.

GASES AND LIQUIDS

Detailed Comparative Analysis of Interaction of a Supersonic Flow with a Transverse Gas Jet at High Pressure Ratios

A. O. Beketaeva[a,*,**], **P. Bruel**[b], **and A. Zh. Naimanova**[c]
[a] *Al-Farabi Kazakh National University, Almaty, 050040 Kazakhstan*
[b] *CNRS—University Pau & Pays Adour, LMAP—Inria CAGIRE Team, 64 013 Pau, France*
[c] *Institute of Mathematics and Mathematical Modeling, Ministry of Education and Science of Republic of Kazakhstan, Almaty, 050010 Kazakhstan*
**e-mail: azimaras10@gmail.com*
***e-mail: azimaras@mail.ru*

Received January 17, 2019; revised January 17, 2019; accepted April 24, 2019

Abstract—The interaction of a 3D supersonic turbulent gas flow with a transverse sonic jet injected from the wall has been studied in detail both numerically and experimentally. However, the main drawback of such studies is the lack of detailed description of formation and propagation of vortex structures for moderate and large parameters n (ratio of pressure in the jet to pressure in the flow). Analysis performed in this study is aimed at revelation and detailed explanation of mechanisms of formation of vortices behind the injected sonic jet in a supersonic oncoming flow depending on n for improving the effectiveness of mixing of the jet with the flow. As initial equations, we have used 3D Favre-averaged Navier–Stokes equations closed by the k–ω model of turbulence; these equations are solved using the algorithm based on the essentially nonoscillatory scheme of the third approximation order. We have demonstrated the presence of the following vortex structures known from a number of theoretical publications: two oppositely rotating vortices in front of the jet, a horseshoe vortex; and two pairs formed in the mixing zone between the jet and the flow (one in the wake behind the jet and the other on the lateral line of the jet). We have determined the pressure ratios for which extra pairs of vortices appear (one pair emerges at the Mach disk edge as a result of interaction of a retarded flow of the jet behind the Mach disk with a high-velocity ascending flow behind the barrel and the other pair is formed due to the interaction of the ascending jet flow with the incoming main gas flow). As a result of comparative analysis, the pressure ratios for which a clear pattern of additional horn vortices is observed near the wall in the region behind the jet, have been determined. The dependence of the slope of the bow shock on the pressure ratio has been plotted. It is found that the pressure distribution at the wall in front of the jet in the symmetry plane is in satisfactory agreement with experimental data.

DOI: 10.1134/S1063784219100049

INTRODUCTION

The flows of high-velocity jets in a transverse flow ensure effective mixing of the fuel and the oxidizer, which is critical for supersonic combustion. At present, the mechanism of formation of the shock-wave structure of jet interaction has been studied comprehensively in several experimental [1–5] and theoretical [6–14] works for moderate parameters n (ratio of pressures in the jet and in the flow). The general pattern of the flow can be represented schematically as follows (flow diagram in Fig. 1a and on the symmetry line in Fig. 1b): bow shock (*1*) emerging due to deceleration of the incoming flow in front of the jet and (*2*, *3*) oblique and terminal shocks, respectively. The bow, oblique, and terminal shocks intersecting at one point form a λ-shaped structure. The Mach disk and the barrel structure in the jet are denoted by letters D and B, respectively. Lines *4* and *5* show two well-known oppositely rotating vortices in front of the jet, which appear due to a high-pressure gradient produced on the wall in front of the injected jet and, as a consequence, due to the separation of the boundary layer. Figure 1c illustrates schematically the vortex structure behind the jet, which is known to make a significant contribution to mixing of fuel with an oxidizer. Here, curve *6* represents the vortex trail and *8* is the well-known oppositely rotating pair of vortices in the jet itself, which is formed by the jet sag and convection of the transverse flow; horseshoe vortex *7* is also indicated here.

However, the existence of extra pairs of vortices behind the jet, which is also illustrated in Fig. 1c, was revealed in [9] as a result of numerical simulation of a flow with pressure ratio $n = 282$ and in calculations [13] with pressure ratios from interval $10 \le n \le 50$. In this pattern, *9* and *10* are new vortex structures; pair of vortices *9* appears due to the interaction of the jet pass-

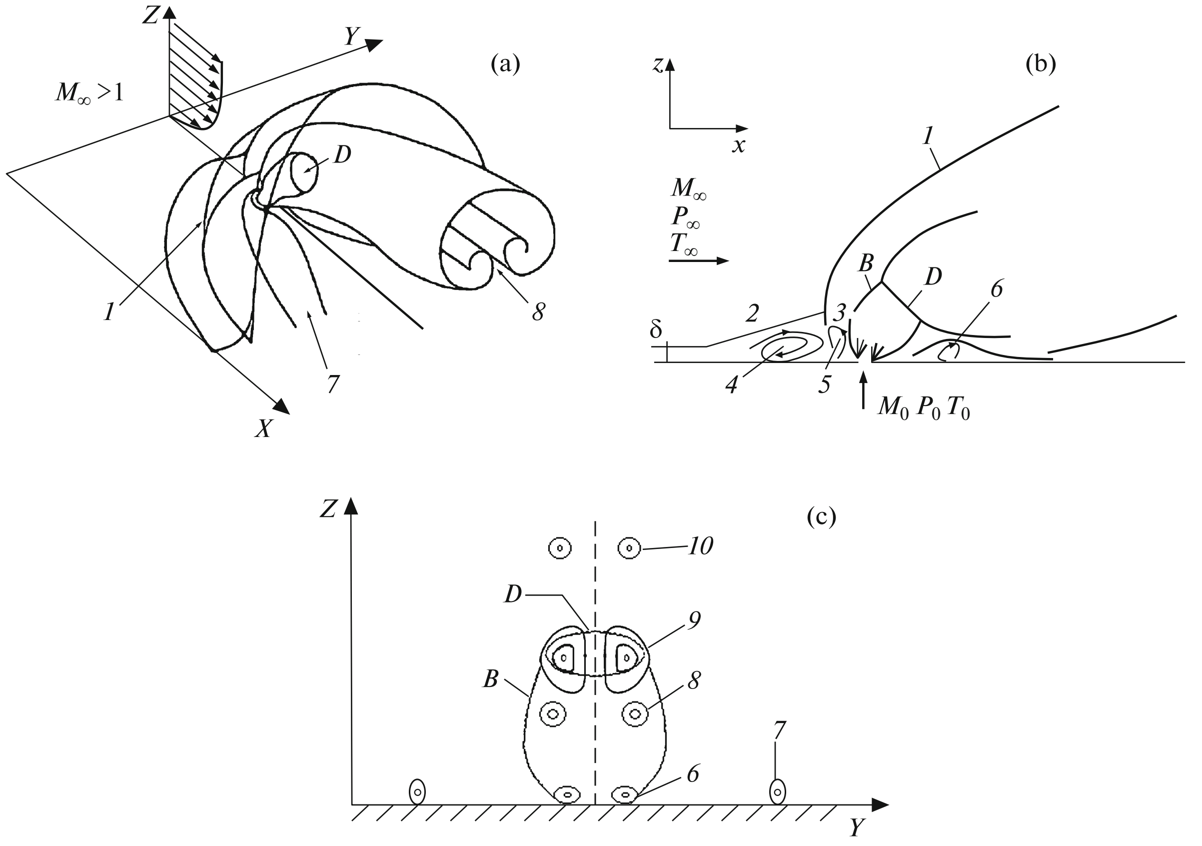

Fig. 1. Flow diagram (explanation is given in the text).

ing through the Mach disk with an ascending external flow, while vortices *10* are generated due to the interaction of the flow with the barrel structure in the jet.

It should also be noted that the results obtained in [10] for pressure ratios $5 \leq n \leq 2000$ confirm the presence of familiar vortices and show additional pair of (horn) vortices behind the injected jet straight at the wall, where the boundary layer streamlines the jet emerging in the subsonic as well as in supersonic flows; however, no such vortices were revealed in [9, 13]. It is difficult to perform comparative analysis for our results and the data from [10] because no quantitative description was given in the latter publication concerning the generation and propagation of vortices. This necessitates further investigation of vortex structures in a wide range of pressure ratios.

This study is aimed at numerical and detailed comparative analysis of the mechanisms of vortex and shock structure formation in a wide range of pressure ratios and at obtaining generalized dependences of characteristics of the flow for various pressure ratios. For this purpose, we simulate the problem of injection of sonic jets from circular holes drilled symmetrically in the upper and lower channel walls perpendicularly to the supersonic flow. For convenience of calculations, we consider the injection of the jet only from the lower wall. The flow diagram and qualitative pattern of the vortex structure are shown schematically in Fig. 1.

1. FORMULATION OF THE PROBLEM

The initial system of equations is represented by the 3D Favre-averaged Navier–Stokes equations for a compressible turbulent gas, which is written in the Cartesian system of coordinates in conservative form:

$$\frac{\partial \mathbf{U}}{\partial t} + \frac{\partial(\mathbf{E} - \mathbf{E}_v)}{\partial x} + \frac{\partial(\mathbf{F} - \mathbf{F}_v)}{\partial z} + \frac{\partial(\mathbf{G} - \mathbf{G}_v)}{\partial y} = \mathbf{S}, \quad (1)$$

components of vectors **U**, **E**, **F**, and **G** are defined as

$$\mathbf{U} = \begin{pmatrix} \rho \\ \rho u \\ \rho v \\ \rho w \\ E_t \\ \rho k \\ \rho\omega \end{pmatrix}, \quad \mathbf{E} = \begin{pmatrix} \rho u \\ \rho u^2 + P \\ \rho uv \\ \rho uw \\ (E_t + P)u \\ \rho uk \\ \rho u\omega \end{pmatrix},$$

$$\mathbf{F} = \begin{pmatrix} \rho w \\ \rho u w \\ \rho v w \\ \rho w^2 + P \\ (E_t + P)w \\ \rho w k \\ \rho w \omega \end{pmatrix}, \quad \mathbf{G} = \begin{pmatrix} \rho v \\ \rho u v \\ \rho v^2 + P \\ \rho v w \\ (E_t + P)v \\ \rho v k \\ \rho v \omega \end{pmatrix},$$

while components $\mathbf{E}_v$, $\mathbf{F}_v$, and $\mathbf{G}_v$ are connected by viscous stresses

$$\mathbf{E}_v = \Bigg(0,\ \tau_{xx}, \tau_{xy}, \tau_{xz}, u\tau_{xx} + v\tau_{xz} + w\tau_{xz} - q_x,$$

$$\frac{1}{\mathrm{Re}}(\mu_l + \sigma_k \mu_t)\frac{\partial k}{\partial x}, \frac{1}{\mathrm{Re}}(\mu_l + \sigma_\omega \mu)\frac{\partial \omega}{\partial x}\Bigg)^{\mathrm{T}},$$

$$\mathbf{F}_v = \Bigg(0,\ \tau_{xz}, \tau_{yz}, \tau_{zz}, u\tau_{xz} + v\tau_{yz} + w\tau_{zz} - q_z,$$

$$\frac{1}{\mathrm{Re}}(\mu_l + \sigma_k \mu_t)\frac{\partial k}{\partial z}, \frac{1}{\mathrm{Re}}(\mu_l + \sigma_\omega \mu)\frac{\partial \omega}{\partial z}\Bigg)^{\mathrm{T}},$$

$$\mathbf{G}_v = \Bigg(0,\ \tau_{xy}, \tau_{yy}, \tau_{yz}, u\tau_{yy} + v\tau_{yy} + w\tau_{yz} - q_y,$$

$$\frac{1}{\mathrm{Re}}(\mu_l + \sigma_k \mu_t)\frac{\partial k}{\partial y}, \frac{1}{\mathrm{Re}}(\mu_l + \sigma_\omega \mu)\frac{\partial \omega}{\partial y}\Bigg)^{\mathrm{T}}.$$

Stress tensors and heat fluxes are given by

$$\tau_{xx} = \frac{2}{3}\frac{\mu}{\mathrm{Re}}\left(2\frac{\partial u}{\partial x} - \frac{\partial w}{\partial z} - \frac{\partial v}{\partial y}\right),$$

$$\tau_{zz} = \frac{2}{3}\frac{\mu}{\mathrm{Re}}\left(2\frac{\partial w}{\partial z} - \frac{\partial u}{\partial x} - \frac{\partial v}{\partial y}\right),$$

$$\tau_{yy} = \frac{2}{3}\frac{\mu}{\mathrm{Re}}\left(2\frac{\partial v}{\partial y} - \frac{\partial u}{\partial x} - \frac{\partial w}{\partial z}\right),$$

$$\tau_{xz} = \tau_{zx} = \frac{\mu}{\mathrm{Re}}\left(\frac{\partial u}{\partial z} + \frac{\partial w}{\partial x}\right),$$

$$\tau_{xy} = \tau_{yx} = \frac{\mu}{\mathrm{Re}}\left(\frac{\partial u}{\partial y} + \frac{\partial v}{\partial x}\right),$$

$$\tau_{yz} = \tau_{zy} = \frac{\mu}{\mathrm{Re}}\left(\frac{\partial w}{\partial x} + \frac{\partial v}{\partial z}\right),$$

$$q_x = \frac{\mu}{(\gamma - 1)M_\infty^2 \,\mathrm{Pr}\,\mathrm{Re}}\frac{\partial T}{\partial x},$$

$$q_y = \frac{\mu}{(\gamma - 1)M_\infty^2 \,\mathrm{Pr}\,\mathrm{Re}}\frac{\partial T}{\partial y},$$

$$q_z = \frac{\mu}{(\gamma - 1)M_\infty^2 \,\mathrm{Pr}\,\mathrm{Re}}\frac{\partial T}{\partial z}.$$

Here, $\mu = \mu_l + \mu_t$, where μ_l is the molecular viscosity (defined by the Sutherland law) and μ_t is the turbulent viscosity.

The vector of supplementary terms has form

$$\mathbf{S} = (0, 0, 0, 0, 0, (P_k - \beta^* \rho\omega k), (\gamma^* \rho P_k/\mu_t - \beta\rho\omega^2))^{\mathrm{T}},$$

where

$$P_k = \mu_t\left[\left(\frac{\partial u_i}{\partial x_j} + \frac{\partial u_j}{\partial x_i}\right)\frac{\partial u_i}{\partial x_j} - \frac{2}{3}\left(\frac{\partial u_k}{\partial x_k}\right)^2\right] - \frac{2}{3}\rho k\frac{\partial u_k}{\partial x_k},$$

$$i, j, k = 1, 2, 3.$$

The constants assume the following values:

$$\sigma_k = 0.5, \quad \sigma_w = 0.5, \quad \beta^* = 0.09,$$
$$\beta = 0.075, \quad \gamma^* = 5/9.$$

Here, k and ω are the kinetic energy of turbulence and turbulent kinetic energy dissipation rate, and P_k is the term describing the generation of turbulence; turbulent viscosity is defined as $\mu_t = \dfrac{\rho k}{\omega}$ [15].

The expressions for the pressure and temperature have form

$$P = (\gamma - 1)\left[E_t - \frac{1}{2}(\rho u^2 + \rho w^2 + \rho v^2)\right],$$

$$T = \left(\frac{1}{\rho c_v}\right)\left[E_t - \frac{1}{2}(\rho u^2 + \rho w^2 + \rho v^2)\right],$$

$$c_v = \frac{1}{\gamma(\gamma - 1)M_\infty^2}.$$

Here, t is time; u, w, and v are the flow velocity components in the longitudinal and transverse directions; ρ is the density; E_t is the total energy; P is the pressure; T is the temperature; c_v is the heat capacity at constant volume; γ is the adiabatic exponent; and M_∞ is the Mach number of the flow; subscripts "0" and "∞" will mark the jet and flow parameters.

Initial system (1) is written in dimensionless form. Key parameters are dimensional parameters $\hat{u}_\infty$, $\hat{\rho}_\infty$, and $\hat{T}_\infty$ at the input; the pressure and total energy are normalized by quantity $\hat{\rho}_\infty \hat{u}_\infty^2$; the characteristic length is diameter $\hat{d}$ of the circular hole for the jet injection; Pr is the Prandtl number, and $\mathrm{Re} = \hat{u}_\infty \hat{\rho}_\infty \hat{L}/\mu$ is the Reynolds number, where $\hat{L}$ is the channel length, which is the key size for Re.

The boundary and initial conditions have the following form: at the inlet, as well as initial data, the parameters of the flow

$$u = 1, \quad v = 0, \quad w = 0, \quad \rho = 1, \quad T_\infty = 1,$$
$$x = 0, \quad 0 \le y \le H_y, \quad 0 \le z \le H_z$$

are specified.

The initial data for parameters k and ω were determined using the Baldwin–Lomax algebraic turbulence model from the known averaged physical parameters of the input flow and were described in detail in [13].

Near the wall, the boundary layer is specified with a thickness defined by formula $\delta_1 = 0.37x(\mathrm{Re})^{-0.2}$. The near-wall layer (10% of the boundary layer, $\delta_2 = 0.1\delta_1$) is also specified. The longitudinal component of velocity u, as well as temperature and densities, are approximated in accordance with [13]: on the jet,

$$u = 1, \quad v = 0, \quad w = \sqrt{T_0}M_0/M_\infty, \quad P_0 = nP_\infty,$$
$$T_0 = 3.71, \quad z = 0, \quad |x^2 + y^2| \le R.$$

Here, $n = P_0/P_\infty$ is the pressure ratio.

At the upper boundary, the symmetry condition is specified:

$$w = 0; \quad \frac{\partial u}{\partial z} = 0; \quad \frac{\partial v}{\partial z} = 0; \quad \frac{\partial T}{\partial z} = 0; \quad \frac{\partial k}{\partial z} = 0;$$
$$\frac{\partial \omega}{\partial z} = 0; \quad z = H_z, \quad 0 \le x \le H_x, \quad 0 \le y \le H_y.$$

At lateral boundaries, we have

$$\frac{\partial u}{\partial y} = \frac{\partial v}{\partial y} = \frac{\partial w}{\partial y} = \frac{\partial \rho}{\partial y} = \frac{\partial k}{\partial y} = \frac{\partial \omega}{\partial y} = 0,$$
$$y = 0, \quad y = H_y, \quad 0 \le x \le H_x, \quad 0 \le z \le H_z,$$

where $H_x = \hat{L}/\hat{d}$ is the length, H_z is the height, H_y is the width of the dimensionless computation domain, and $R = 0.5$ is the circular hole radius; at the outlet boundary, the nonreflection condition is specified [16].

2. METHOD OF SOLUTION

In [17, 18], the essentially nonoscillatory (ENO) scheme based on the Godunov method was described and its applicability to solving the problem of supersonic multicomponent gas flow in a plane channel with injection of transverse jets was demonstrated. The algorithm developed in [17, 18] was generalized in [13] to the 3D case, and the possibility of reliable calculations of complex supersonic 3D flows was demonstrated. In this algorithm, the grid concentration is preliminarily introduced in the boundary layer near the wall at the jet level for more exact analysis of the flow using the following transformations:

$$\xi = \xi(x), \quad \eta = \eta(z), \quad \zeta = \zeta(y). \tag{2}$$

In this case, system of equations (1) in generalized coordinates can be written in form

$$\begin{aligned}\frac{\partial \hat{\mathbf{U}}}{\partial t} + \frac{\partial \hat{\mathbf{E}}}{\partial \xi} + \frac{\partial \hat{\mathbf{F}}}{\partial \eta} + \frac{\partial \hat{\mathbf{G}}}{\partial \zeta} &= \frac{\partial \hat{\mathbf{E}}_{v2}}{\partial \xi} + \frac{\partial \hat{\mathbf{E}}_{vm}}{\partial \xi} + \frac{\partial \hat{\mathbf{F}}_{v2}}{\partial \eta} \\ &+ \frac{\partial \hat{\mathbf{F}}_{vm}}{\partial \eta} + \frac{\partial \hat{\mathbf{G}}_{v2}}{\partial \zeta} + \frac{\partial \hat{\mathbf{G}}_{vm}}{\partial \zeta},\end{aligned} \tag{3}$$

where

$$\tilde{\mathbf{U}} = \frac{1}{J}\mathbf{U}, \quad \tilde{\mathbf{E}} = \left(\frac{\xi_x}{J}\right)\mathbf{E}, \quad \tilde{\mathbf{F}} = \left(\frac{\eta_z}{J}\right)\mathbf{F},$$
$$\tilde{\mathbf{E}}_{v2} = \left(\frac{\xi_x}{J}\right)\mathbf{E}_{v2}, \quad \tilde{\mathbf{E}}_{vm} = \left(\frac{\xi_x}{J}\right)\mathbf{E}_{vm},$$
$$\tilde{\mathbf{F}}_{v2} = \left(\frac{\eta_z}{J}\right)\mathbf{F}_{v2}, \quad \tilde{\mathbf{F}}_{vm} = \left(\frac{\eta_z}{J}\right)\mathbf{F}_{vm},$$
$$\tilde{\mathbf{G}}_{v2} = \left(\frac{\zeta_y}{J}\right)\mathbf{G}_{v2}, \quad \tilde{\mathbf{G}}_{vm} = \left(\frac{\zeta_y}{J}\right)\mathbf{G}_{vm},$$
$$J = \frac{\partial(\xi, \eta, \zeta)}{\partial(x, z, y)}$$

is the Jacobian of the transformation, and $\tilde{\mathbf{E}}_{vm}$ and $\tilde{\mathbf{E}}_{v2}$ are the diffusion terms containing mixed and second derivatives.

In accordance with the principle of constructing the ENO scheme, the initial system of equations is formally represented as

$$\begin{gathered}\frac{\partial \tilde{\mathbf{U}}}{\partial t} + (\hat{A}^+ + \hat{A}^-)\frac{\partial \mathbf{E}^m}{\partial \xi} \\ + (\hat{B}^+ + \hat{B}^-)\frac{\partial \mathbf{F}^m}{\partial \eta} + (\hat{Q}^+ + \hat{Q}^-)\frac{\partial \mathbf{G}^m}{\partial \zeta} \\ - \left[\frac{\partial(\tilde{\mathbf{E}}_{v2} + \tilde{\mathbf{E}}_{vm})}{\partial \xi} + \frac{\partial(\tilde{\mathbf{F}}_{v2} + \tilde{\mathbf{F}}_{vm})}{\partial \eta} - \frac{\partial(\tilde{\mathbf{G}}_{v2} + \tilde{\mathbf{G}}_{vm})}{\partial \zeta}\right] = 0.\end{gathered} \tag{4}$$

Here,

$$A = \frac{\partial \mathbf{E}}{\partial \mathbf{U}}, \quad B = \frac{\partial \mathbf{F}}{\partial \mathbf{U}}, \quad Q = \frac{\partial \mathbf{G}}{\partial \mathbf{U}}$$

are the Jacobi matrices,

$$\hat{A}^\pm = R\hat{\Lambda}_\xi R^{-1} = R\left(\frac{1 \pm \mathrm{sgn}(\Lambda_\xi)}{2}\right)R^{-1},$$
$$\hat{B}^\pm = T\hat{\Lambda}_\eta T^{-1} = T\left(\frac{1 \pm \mathrm{sgn}(\Lambda_\eta)}{2}\right)T^{-1},$$
$$\hat{Q}^\pm = S\hat{\Lambda}_\zeta S^{-1} = S\left(\frac{1 \pm \mathrm{sgn}(\Lambda_\zeta)}{2}\right)S^{-1},$$

$\mathbf{E}^m = \tilde{\mathbf{E}} + \mathbf{E}_\xi + \mathbf{D}_\xi$, $\mathbf{F}^m = \tilde{\mathbf{F}} + \mathbf{E}_\eta + \mathbf{D}_\eta$, and $\mathbf{G}^m = \tilde{\mathbf{G}} + \mathbf{E}_\zeta + \mathbf{D}_\zeta$ are modified fluxes at nodal points (i, j, k), which consist of initial convective vectors ($\tilde{\mathbf{E}}$, $\tilde{\mathbf{F}}$, $\tilde{\mathbf{G}}$) and additional higher-order terms ($\mathbf{E}_\xi$, $\mathbf{D}_\xi$, $\mathbf{E}_\eta$, $\mathbf{D}_\eta$, $\mathbf{E}_\zeta$, and $\mathbf{D}_\zeta$), which are described in detail in [17, 18].

After factorization of the one-step finite-difference scheme for integration of Eq. (4) with respect to time, we obtain the following equality:

$$\left\{I + \Delta t\left[(\hat{A}^+ + \hat{A}^-)^n \frac{\partial}{\partial \xi} A_\xi^n \bullet - \frac{\partial}{\partial \xi}\tilde{\mu}_\xi \frac{\partial}{\partial \xi}\frac{1}{\tilde{\mathbf{U}}_I} \bullet\right]\right\}$$

$$\times\left\{I+\Delta t\left[(\hat{B}^{+}+\hat{B}^{-})^{n}\frac{\partial}{\partial\eta}B_{\eta}^{n}\bullet-\frac{\partial}{\partial\eta}\tilde{\mu}_{\eta}\frac{\partial}{\partial\eta}\frac{1}{\tilde{\mathbf{U}}_{I}}\bullet\right]\right\}$$

$$\times\left\{I+\Delta t\left[(\hat{Q}^{+}+\hat{Q}^{-})^{n}\frac{\partial}{\partial\zeta}Q_{\zeta}^{n}\bullet-\frac{\partial}{\partial\zeta}\tilde{\mu}_{\zeta}\frac{\partial}{\partial\zeta}\frac{1}{\tilde{\mathbf{U}}_{I}}\bullet\right]\right\}\tilde{\mathbf{U}}^{n+1}$$

$$=\tilde{\mathbf{U}}^{n}+\Delta t\left[\frac{\partial\tilde{\mathbf{E}}_{v22}^{n}}{\partial\xi}+\frac{\partial\tilde{\mathbf{F}}_{v22}^{n}}{\partial\eta}+\frac{\partial\tilde{\mathbf{G}}_{v22}^{n}}{\partial\zeta}+\frac{\partial}{\partial\xi}(2\tilde{E}_{vm}^{n}-\tilde{\mathbf{E}}_{vm}^{n-1})\right. \tag{5}$$

$$\left.+\frac{\partial}{\partial\eta}(2\tilde{F}_{vm}^{n}-\tilde{\mathbf{F}}_{vm}^{n-1})+\frac{\partial}{\partial\zeta}(2\tilde{G}_{vm}^{n}-\tilde{\mathbf{G}}_{vm}^{n-1})\right]$$

$$-\Delta t\left[(\hat{A}^{+}+\hat{A}^{-})\frac{\partial}{\partial\xi}(\mathbf{E}_{\xi}+\mathbf{D}_{\xi})+(\hat{B}^{+}+\hat{B}^{-})\frac{\partial}{\partial\eta}(\mathbf{E}_{\eta}+\mathbf{D}_{\eta})\right.$$

$$\left.+(\hat{Q}^{+}+\hat{Q}^{-})\frac{\partial}{\partial\zeta}(\mathbf{E}_{\zeta}+\mathbf{D}_{\zeta})\right]^{n},$$

where $A_{\xi}=\xi_{x}A$, $B_{\eta}=\eta_{z}B$, and $Q_{\zeta}=\zeta_{y}Q$, and $\hat{A}^{+}+\hat{A}^{-}=I$, I being the identity matrix, and

$$\tilde{\mu}_{\xi}=\frac{\mu\xi_{x}^{2}}{\mathrm{Re}\,J},\quad \tilde{\mu}_{\eta}=\frac{\mu\eta_{z}^{2}}{\mathrm{Re}\,J},\quad \tilde{\mu}_{\zeta}=\frac{\mu\zeta_{y}^{2}}{\mathrm{Re}\,J}.$$

The derivatives in the convective terms, terms containing additional high-order vectors, as well as terms containing the second and mixed derivatives are approximated in accordance with [17, 18]. System (5) is solved using the splitting method in vector $\tilde{\mathbf{U}}$ by matrix sweep.

3. ANALYSIS OF RESULTS

We analyze the supersonic flow with parameters $\mathrm{Pr}=0.72$, $\mathrm{Re}=1.87\times10^{6}$, $M_{\infty}=4$, and $\hat{T}_{\infty}=70.3$ K past an ideal gas sonic jet flow ($M_0=1$) through a hole of diameter $\hat{d}=0.476$ cm at $\hat{T}_0=261$ K with pressure ratios in the interval $50\le n\le300$ in a channel of length 27.69 cm, height of 11.43 cm, and width of 15.24 cm. The dimensionless parameters of computation domain were as follows: $H_x=58$, $H_y=32$, and $H_z=24$, where the distance from the input boundary to the injected jet center is $x_0=16$, $y_0=16$. The height of the boundary layer at the inlet was $\delta_1=1.65$, where 22–26 mesh points of the grid were used for this height. The range of the pressure ratio considered here was $50\le n\le300$. Detailed analysis of the convergence of numerical solution based on the proposed technique was performed in [13] using as an example the solution of the 3D problem of the transverse injection of a sonic jet with moderate pressure ratios. Accordingly, we chose the grid of size 251 × 121 × 151.

Figures 2–6 demonstrate the results of numerical simulation with pressure ratio $n=300$. The velocity vector field shown in Fig. 2a shows that two oppositely rotating vortices *4* and *5* are formed in front of the jet analogously to the case with moderate pressure ratios; these vortices appear as a result of detachment of the incoming flow induced by the λ-shaped system of shocks. These vortices are clearly seen in Fig. 2b showing the projection of the flow lines onto the plane normal to the y axis in the symmetry plane ($y=16$). Figure 2c shows the isobars for the λ-shaped system of shock waves (bow, oblique, and terminal shocks).

Figure 2a also shows the dependence of pressure coefficient C_p at the wall (solid curve), which indicates that as we approach the injection region, the pressure increases, and then its growth slows down so that a small plateau is formed (region I). Further, it can be seen that pressure decreases (region II), and the velocity vector field indicates that pressure region II corresponds to the core of horseshoe vortex *4*, and its minimal value corresponds to the center of rotation. The region of pressure drop is followed by a sharp increase in the pressure coefficient (region III), where it reaches its maximal value (region IV). Numerical calculations show that the pressure maximum is the zone of separation of rotating vortices *4* and *5* (see Fig. 2a). The correspondence of the pressure peak to the vortex separation zone can be explained by the fact that the air flow passing through the regions of the λ-shaped system of shocks (in particular, the terminal shock) behind which the pressure attains the highest value turns downwards to the wall and penetrates the region of the separated flow, and then spreads in opposite directions with the formation of two vortices, vortex *4* moving clockwise and vortex *5*, counterclockwise. The isobar distribution curves (see Fig. 2b) show that the pressure peak lies behind the lower part of the terminal shock (pressure equals 1.5). Figure 2d demonstrates the distribution of vorticity $\omega=|\mathrm{curl}(\mathbf{u})|$ in which the barrel-shaped structure formed during the injection of the underexpanded jet into the supersonic flow; high values of vorticity can also be seen in the figure in the presence of the aforementioned vortices.

The left part in Fig. 3a (velocity vector field and pressure coefficient C_p in the xz plane, $y=18.41$) demonstrates the lateral spreading of vortices *4* and *5*. It can be seen that the two vortices are separated by the maximal pressure on the C_p curve (region IV). It can be seen that vortex *5* has a blurred structure (right part of Fig. 3a shows the projections of the flow lines onto the plane normal to the x axis) and that it is enhanced by the upward flow. In all probability, the center of rotation of vortex *5* is reoriented in this region.

With increasing distance from the symmetry line, vortices *4* and *5* are substantially rearranged. Beginning with section $y=18.74$, only vortex *4* can be seen. Then, its core splits into two cores (Fig. 3b, xz plane, $y=20.97$). As follows from the figure, the maximal value of C_p does not correspond to the zone of separation of two vortices, which suggests the bifurcation of vortex *4*. The split vortex rapidly disintegrates (Fig. 3c, xz plane, $y=22.98$); in this region, there is only one vortex. Further, beginning from section $y=24.25$,

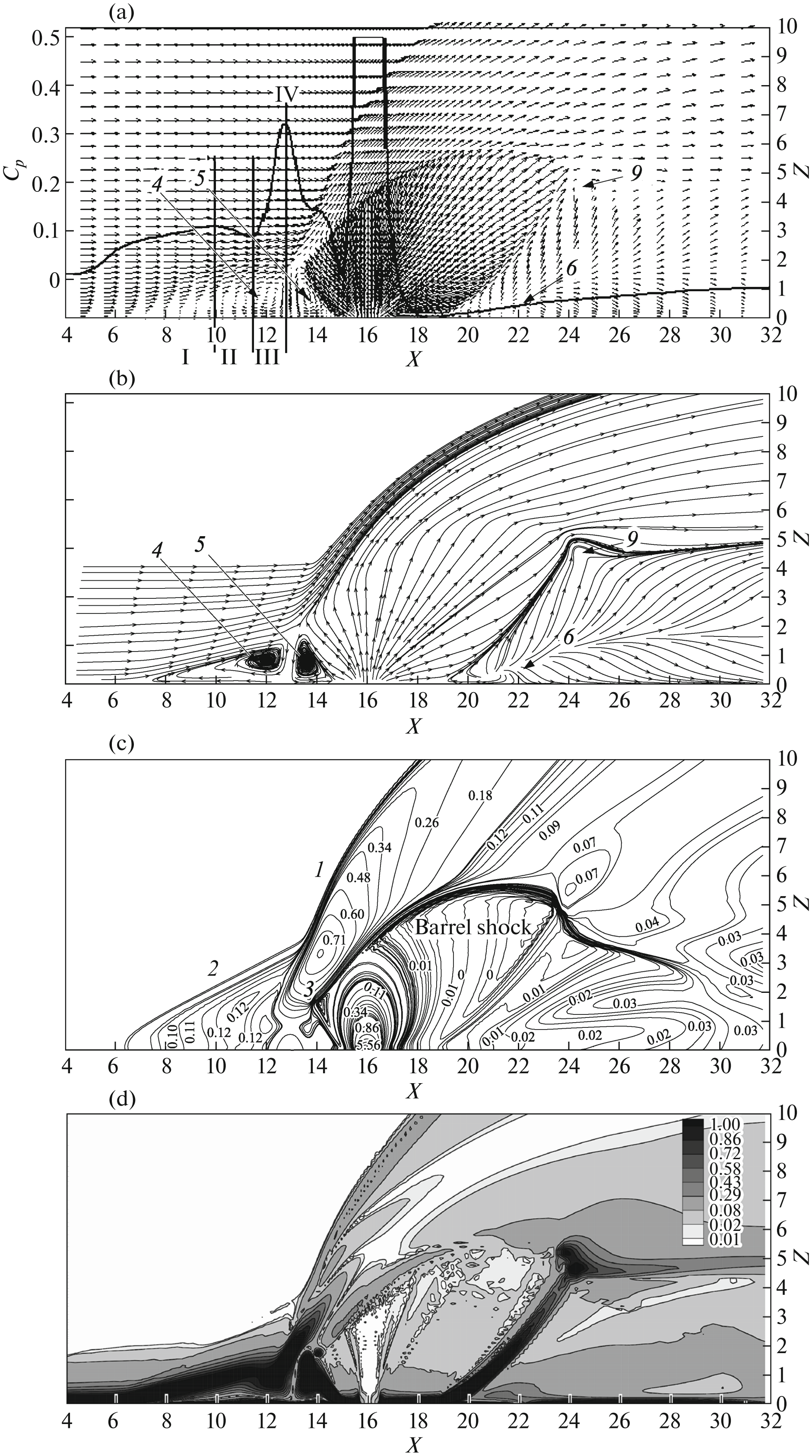

Fig. 2. (a) Velocity vector field and pressure coefficient C_p at the wall; (b) projections of flow lines onto the plane normal to the y axis; (c) isobars; (d) vorticity for Re = 1.87×10^6, Pr = 0.72, $n = 300$, $M_0 = 1$, and $M_\infty = 4$ in the symmetry plane (section $y = 16$).

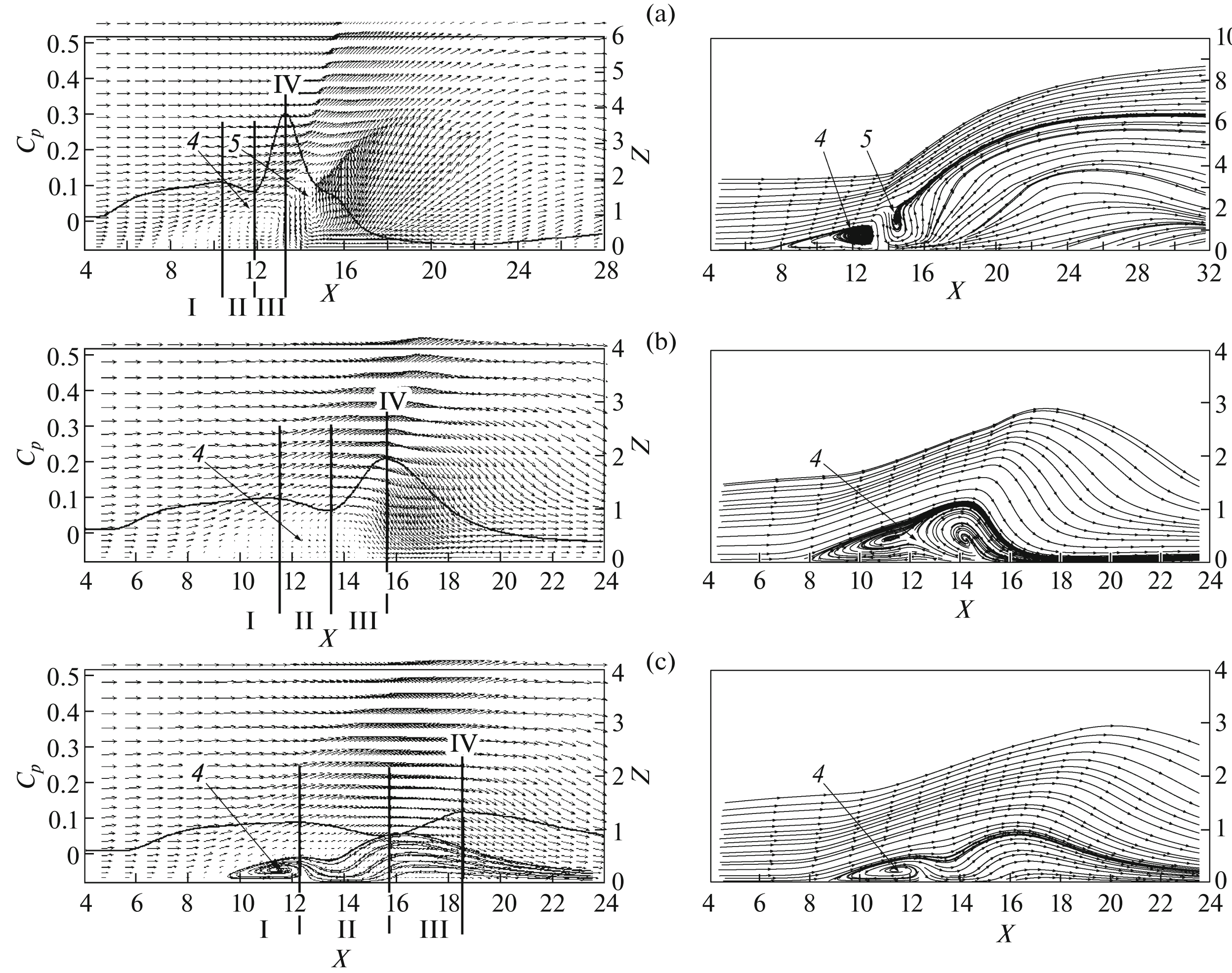

Fig. 3. (left) Velocity vector field and pressure coefficient C_p at the wall; (right) projections of flow lines onto the plane normal to the y axis for $\mathrm{Re} = 1.87 \times 10^6$, $\mathrm{Pr} = 0.72$, $n = 300$, $M_0 = 1$, and $M_\infty = 4$ in the zx plane: (a) section $y = 18.41$; (*b*) $y = 20.97$, and (c) $y = 22.98$.

vortex structure *4* cannot be seen any longer; apparently, reorientation of the center of rotation and its alignment in the direction of the transverse flow also occur in this region.

Figure 4a (yz plane, section $x = 17$) shows pair of vortices *8* generated by vortex *5* as a result of lateral flow [13]. The left part of the figure shows that vorticity $\omega = |\mathrm{curl}(\mathbf{u})|$ has high values in the region in which vortex *8* is present. Computer experiments show that in the case considered here, this pair of vortices possesses (like in the case of moderate values of $n = 50$ [13]) a high energy, which allows these vortices not only to move downstream, but also to increase in size. Numerical results show that the maximal sizes of the lateral vortex are observed for $x = 22.85$. Analogously to [13], we believe that the increase in size of these vortices is apparently due to their localization in the wall region, and the increase in the boundary layer thickness also facilitates their growth. It follows from the results of numerical calculations that beginning from this section, the intensity of lateral vortices *8* decreases, and the barrel structure in the jet disappears. Upon the downstream propagation of vortex *8*, its intensity in the transverse direction decreases, and it is not observed in sections from $x = 23.24$ to $x = 26.90$.

Figure 4b (plane yz, $x = 26.30$) shows vortex pair *9* that is formed at the base of the Mach disk as a result of interaction of the jet with the upward flow. In this region, vortex trail *6* is observed near the wall in the low-pressure region. The vorticity in the graph in the region of vortices *9* and *6* is also high. The presence of these vortex pairs and the mechanisms of their formation were studied in [13] for moderate pressure ratios in the range $10 \le n \le 50$ and in [9] for $n = 282$. Therefore, the vortex structure described above is quite stable. The vorticity distribution indicates the presence of horseshoe vortex *7* in the region of moderate values of vorticity, which are localized in the near-wall region.

The pattern in which newly intensified vortex *8* rotates in pair with vortex *9* is shown in Fig. 4c in sec-

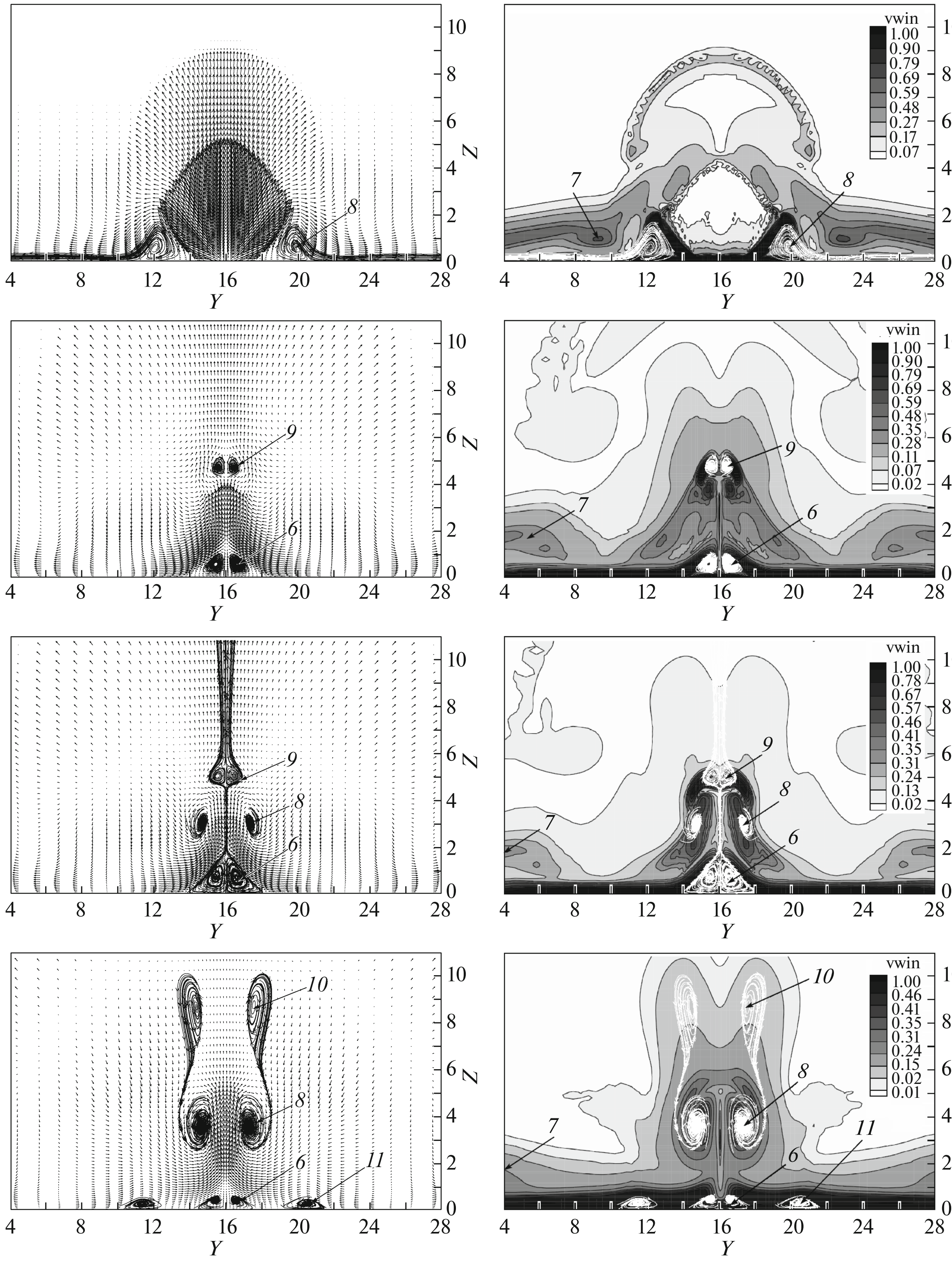

Fig. 4. (left) Velocity vector field and projections of flow lines onto the plane normal to the x axis and (right) vorticity for Re = 1.87 × 10^6, Pr = 0.72, n = 300, M_0 = 1, and M_∞ = 4 in the zy plane: (a) section x = 17; (b) 26.30; (c) 28.18, and (d) 42.32.

tion $x = 28.18$. It should be noted that for pressure ratio $n = 282$, the author of [9] obtained this structure with two vortices in section $x = 31$, while in numerical calculations for the same pressure ratio, this value appeared in section $x = 26.90$. The results coincide qualitatively, while the quantitative discrepancy can be

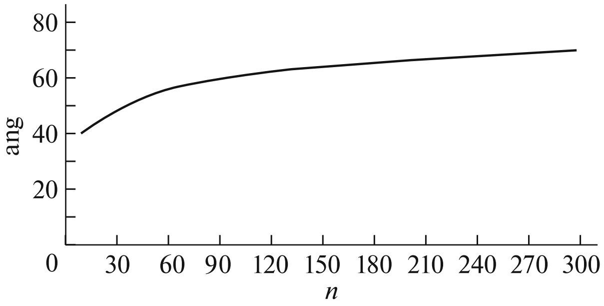

Fig. 5. Influence of the pressure ratio on the tilt of the bow shock.

explained by different formulations of the initial boundary conditions for x and ω in the model of turbulence. The same figure demonstrates an increase in the size of vortex pair *6*.

Further, beginning from section $x = 30.05$, vortex *9* is entrained by vortex *8*. This follows from the fact that the direction of rotation of the formed vortex coincides with direction of rotation of vortex *8* and is preserved to the end of the computation domain.

Figure (*zy* plane, $x = 42.32$) confirms the presence of vortex pair *10*, which was detected numerically for

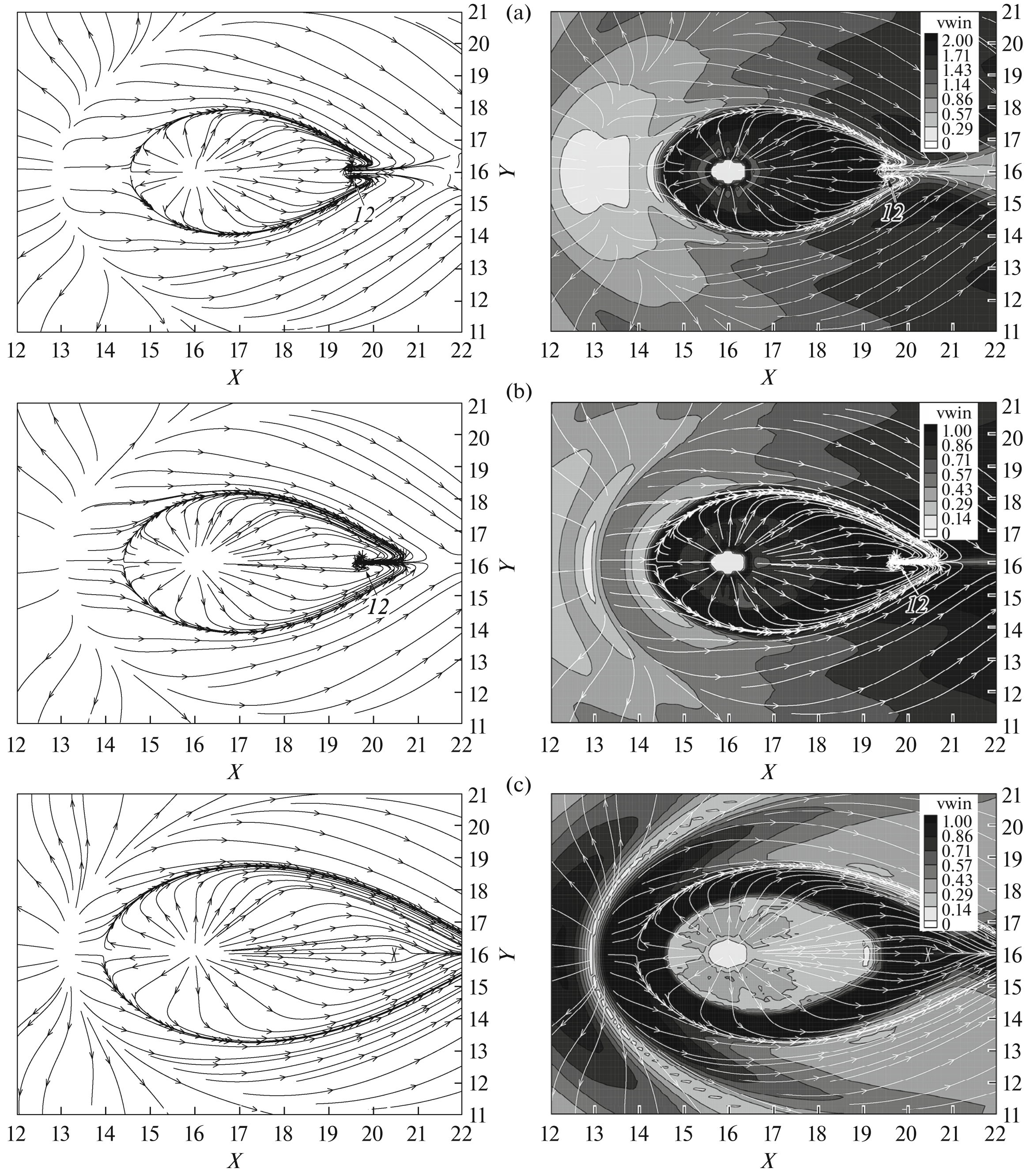

Fig. 6. (left) Projections of flow lines onto the plane normal to the z axis and (right) vorticity for Re = 1.87×10^6, Pr = 0.72, n = 300, $M_0 = 1$, and $M_\infty = 4$ in the xy plane: (a) section $z = 0.1235$; (b) 0.2648; and (c) 0.5958.

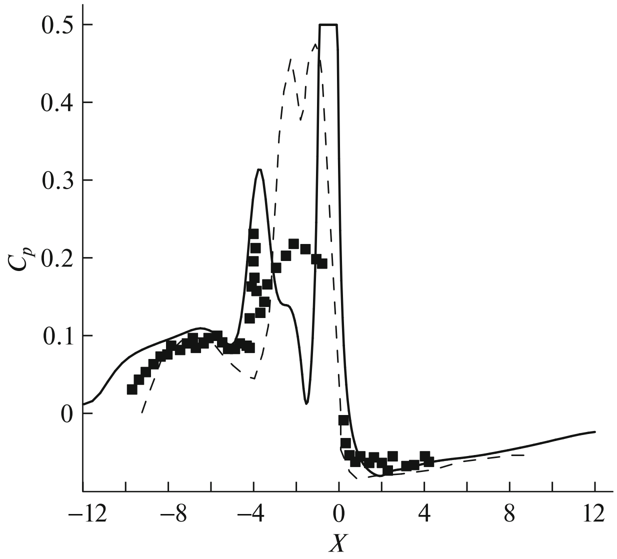

Fig. 7. Distribution of pressure coefficient C_p at the wall on the symmetry axis for Re = 1.87×10^6, Pr = 0.72, $n = 282$, $M_0 = 1$, and $M_\infty = 4$: (solid curve) numerical results; (symbols) experiment [9]; and (dashed curve) results obtained in [9].

the first time in [9] for $n = 282$ and also in [13] for moderate pressure ratios ($n = 50$). It is known that this vortex is formed as a result of interaction of the jet and the high-speed incoming flow passing above the injected jet and appears for pressure ratios exceeding 20.

The same figure demonstrates the emergence of vortex *11* formed as a result of sticking of the jet to the plate plane and described in detail in [13]; it follows from the figure that the direction of its rotation coincides with the direction of trail *6*. Numerical experiments show that vortices *11* and *6* subsequently merge together, and only one vortex trail is observed downstream of the flow. The vorticity distribution pattern shows that horseshoe vortex *7* is separated by a large distance from the symmetry line in the range of moderate values of pressure ratio.

It should be noted that the localization of vortex *10* over the height directly depends on the intensity of jet injection and on the shock-wave structure. For example, for moderate pressure ratios (see [13], $n = 50$), this vortex is formed at a height from 4 to 5 units. In the given case, the localization of its center turned out to be at level of $z = 8.7$, while for $n = 282$, it was at height $z = 8.5$. Since vortex *10* is between the jet being injected and the bow shock, its height directly depends on the tilt angle of the bow shock wave. Figure 5 demonstrates the effect of the pressure ratio on the bow shock; the abscissa axis corresponds to pressure ratio, while the ordinate axis corresponds to the tilt angle of the bow shock calculated by formula

$$\mathrm{ang} = \arctan\left(\max\frac{w}{u}\right).$$

It can be seen that the tilt angle of the bow shock increases with the ratio of pressures in the jet and in the flow. The tilt angle at small and moderate values of pressure ratio increases sharply; however, beginning with $n = 150$, the angle values remain almost unchanged, and the height of localization of vortices *10* changes insignificantly; i.e., beginning with $n = 150$, the height of localization of these vortices almost remains constant.

In Fig. 6a, in the *xy* plane ($z = 0.1235$), vortices *12* formed near the wall can clearly be seen in the region behind the jet at a small distance from the hole (in section $x = 19.5$). These vortices were described in [10] and were called horn vortices. The physical mechanism of their formation can be described as follows: the jet flowing directly from a hole interacts with the external flow, which streamlines the jet, striving to close on the symmetry line; this leads to twisting of counterpropagating flows in the form of two horn structures. Numerical calculations show that this vortex is also formed for pressure ratio $n = 5$, indicating the stability of the given vortex system. Numerical calculations show that in section $z = 0.2648$ (Fig. 6b), vortices close on the symmetry line, and no horn structures are seen even for $z = 0.5958$ (Fig. 6c).

In Fig. 7, the numerical results for pressure coefficient C_p at the wall in the symmetry plane are compared with the results obtained in [9]. As can be seen, numerical results are in satisfactory agreement with experimental data. A slight discrepancy between the calculated and experimental results in the range $-4 < x < -1$ is apparently due to the use of the k–ω turbulence model, which has probably affected the region of joining of the injected jet with the main flow near the wall, necessitating further modification of the model. This is also confirmed in publication [14] devoted to jet interaction. In this study, we analyzed the applicability of various turbulence models, namely, the Spalart–Allmaras, k–ε, k–ω, and SST models for solving analogous problems based on comparison of calculated and experimental data. It was shown that the use of different models of turbulence leads to different numerical results on the pressure distribution on the wall in front of the injected jet. In particular, calculations based on the k–ω turbulence model lead to underestimated results of numerical simulation as compared to the experiment in the region close to the injected jet also.

CONCLUSIONS

We have performed detailed comparative analysis of formation mechanisms of vortex structures as a result of interaction of the incoming flow with the injected jet for moderate and large pressure ratios $50 \le n \le 300$. It is found that beginning with $n = 50$, the centers of rotation of vortices *4* and *5* are reoriented in the direction of the transverse flow (as a result, their visualization is difficult in sections transverse to the incoming flow) and horseshoe vortex *4* splits into two independent vortex structures upon an increase in the distance from the symmetry line. We have confirmed the presence of horn vortices near the wall in the region behind the jet in the range of pressure ratios $10 \leq n \leq 300$, which are formed as a result of interaction of the jet with the external flow leading to twisting of counterpropagating flows behind the jet in the form of two horn structures. In constructing the generalized dependence of the bow shock tilt angle on the pressure ratio, we have demonstrated a moderately linear increase in this angle for large pressure ratios.

FUNDING

This study was supported by the Ministry of Education and Science of the Republic of Kazakhstan under the grant financing program “Numerical Simulation of Spatial Turbulent Compressible Flows with Injection of Jet and Solid Particle,” 2018–2020, identification no. AP05131555.

CONFLICTS OF INTEREST

The authors claim that there are no conflicts of interest.

REFERENCES

1. A. I. Glagolev, A. I. Zubkov, and Yu. A. Panov, Izv. Akad. Nauk SSSR, Mekh. Zhidk. Gaza, No. 3, 97 (1967).
2. F. W. Spaid and E. E. Zukoski, AIAA J. **6**, 205 (1968).
3. J. A. Schetz, J. Spacecr. Rockets **7**, 143 (1970).
4. S. Aso, K. Inoue, K. Yamaguchi, and Y. Tani, Acta Astronaut. **65**, 687 (2009).
5. W. M. Van Lerberghe, J. G. Santiago, J. C. Dutton, and R. P. Lucht, AIAA J. **38**, 470 (2000).
6. C. F. Chenault and P. S. Beran, AIAA J. **37**, 1257 (1999).
7. D. Sun, C. Hu, and T. Cai, Appl. Math. Mech. **23**, 107 (2002).
8. E. H. Khali and Y. Yao, *Proc. 53rd AIAA Aerospace Sciences Meeting, Kissimmee, United States, 2015.* https://doi.org/10.2514/6.2015-0545
9. V. Viti, R. Neel, and J. Schetz, Phys. Fluids **21**, 046101 (2009).
10. F. K. Lu and D. A. Dickmann, *Proc. 12th French Congress on Visualization in Fluid Mechanics, Nice, France, 2008.* https://pdfs.semanticscholar.org/6ebc/4e4762cb500d-7a48cbd442ce09f1846eae2.pdf.
11. A. O. Beketaeva and A. Zh. Naimanova, J. Appl. Mech. Tech. Phys. **52**, 896 (2011). https://doi.org/10.1134/S0021894411060071
12. W. Huang, J. Tan, J. Liu, and L. Yan, Acta Astronaut. **117**, 142 (2015).
13. A. O. Beketaeva, P. Bruel, and A. Zh. Naimanova, J. Appl. Mech. Tech. Phys. **56**, 777 (2015). https://doi.org/10.1134/S0021894415050041
14. K. N. Volkov, V. N. Emelyanov, and M. C. Yakovchuk, J. Appl. Mech. Tech. Phys. **56**, 789 (2015). https://doi.org/10.1134/S0021894415050053
15. D. C. Wilcox, AIAA Paper No. 93-2905 (Orlando, 1993).
16. T. J. Poinsot and S. K. Lele, J. Comput. Phys. **101**, 104 (1992).
17. A. O. Beketaeva and A. Zh. Naimanova, Vychisl. Tekhnol. **12** (4), 17 (2007).
18. P. Bruel and A. Zh. Naimanova, Thermophys. Aeromech. **17**, 531 (2010).

Translated by N. Wadhwa